

RESEARCH ARTICLE

NANOMATERIALS

Carbon nanotube fibers with dynamic strength up to 14 GPa

Xinshi Zhang^{1,2†}, Xudong Lei^{3,4†}, Xiangzheng Jia^{5†}, Tongzhao Sun^{2,6}, Jiajun Luo^{1,2}, Shichen Xu^{1,2}, Lijun Li², Dan Yan^{1,2}, Yuanlong Shao^{1,2}, Zhenzhong Yong^{7,8,9}, Yongyi Zhang^{7,8,9*}, Xianqian Wu^{3,4*}, Enlai Gao^{5*}, Muqiang Jian^{2*}, Jin Zhang^{1,2*}

High dynamic strength is of fundamental importance for fibrous materials that are used in high-strain rate environments. Carbon nanotube fibers are one of the most promising candidates. Using a strategy to optimize hierarchical structures, we fabricated carbon nanotube fibers with a dynamic strength of 14 gigapascals (GPa) and excellent energy absorption. The dynamic performance of the fibers is attributed to the simultaneous breakage of individual nanotubes and delocalization of impact energy that occurs during the high-strain rate loading process; these behaviors are due to improvements in interfacial interactions, nanotube alignment, and densification therein. This work presents an effective strategy to utilize the strength of individual carbon nanotubes at the macroscale and provides fresh mechanism insights.

Ultrahigh dynamic strength and energy-absorbing fibrous materials are needed in high-strain rate applications, such as ballistic impact and untraceable debris impact on aircraft and spacecraft (1, 2). The impact resistance of fibrous materials is closely related to the hierarchical structures, starting from individual building blocks at the nanoscale, then moving to microfibrils, and finally to the macroscopic ensembles, which provide various methods to dissipate the mechanical energy. A few high-performance fibers, such as ultrahigh-molecular weight polyethylene (UHMWPE), poly(*p*-phenylene-2,6-benzobisoxazole) (PBO), and aramid fibers (3, 4), have been developed and play vital roles in modern industries. Despite these achievements, the fabrication of higher-performance fibers is

still driven by increasing industrial demands. One promising route is the assembly of ultrahigh-performance nanomaterials into macroscopic architectures (5, 6).

Carbon nanotubes (CNTs) with an intrinsic strength of more than 100 GPa (7, 8) have been considered as promising building blocks for constructing high-performance and multifunctional fibers for applications in both quasi-static and dynamic environments (2, 9–13). For example, Xie *et al.* (2) demonstrated the potential applications of CNT fibers (CNTFs) for high-strain rate environments using a stroboscopic quantification method. Three spinning methods are used to fabricate CNTFs, including wet spinning (14, 15), vertically aligned array spinning (16), and direct aerogel spinning (17). Among them, direct aerogel spinning is promising for the continuous and scalable fabrication of ultrastrong fibers consisting of high-aspect ratio CNTs (18–20). However, the quasi-static and dynamic mechanical properties of CNTFs are limited by the poor interfacial interactions, low nanotube alignment, and high porosity formed in the spinning process (21–24). To solve these issues, various posttreatment approaches have been developed to modify the hierarchical structures of CNTFs (25, 26), including solution densification (27, 28), mechanical treatment (20), and thermal annealing (29). However, the tensile strength of CNTFs (<10 GPa), especially the dynamic strength, is far lower than that of individual CNTs (>100 GPa), indicating that there is still plenty of room for improving the strength of CNTFs.

We developed a strategy that includes progressive stretching, infusion with PBO nanofibers and molecular chains (hereafter PBOs), and mechanical rolling to improve the inter-

facial interactions, nanotube alignment, and densification of CNTFs (Fig. 1A and fig. S1). Briefly, functionalized CNTFs (F-CNTFs) are first immersed in chlorosulfonic acid (CSA) solution containing PBOs and swell visibly owing to the protonation effect (30). Afterward, PBOs are infused into F-CNTFs during the progressive stretching treatment (PBO-CNTFs). Finally, mechanical rolling is used to densify PBO-CNTFs (D-PBO-CNTFs) (31). This approach can be used to continuously produce high-performance tows (Fig. 1B and fig. S2). Our experimental characterizations demonstrate that the as-obtained fibers have a highly ordered and densely packed structure with strong interfacial interactions (Fig. 1, C and D). Consequently, D-PBO-CNTFs exhibit a high quasi-static tensile strength of 8.2 ± 0.2 GPa and a toughness of 170.3 ± 17.9 MJ m⁻³, yielding a 355% increase in the tensile strength and a 106% increase in the toughness compared with F-CNTFs (Fig. 1E). The resultant fibers exhibit a dynamic strength of 14.0 ± 0.7 GPa and a toughness of 462.6 ± 102.1 MJ m⁻³ under a high strain rate of about 1400 s⁻¹, values that are higher than those of commercial fibers (e.g., 7.2 ± 0.8 GPa and 295.0 ± 59.5 MJ m⁻³ for PBO fibers, 4.6 ± 0.2 GPa and 174.6 ± 11.6 MJ m⁻³ for Kevlar 29 fibers tested under the same conditions as D-PBO-CNTFs; Fig. 1E).

Fabrication and structure of CNTFs

We first produced continuous CNTFs by floating catalyst chemical vapor deposition (fig. S3A) (17). The as-spun fibers contained impurities such as metallic catalyst particles and amorphous carbon (fig. S3B). To purify and functionalize these fibers with oxygen-containing functional groups (e.g., hydroxy groups), we adopted the posttreatments of weak oxidation and acid washing (fig. S1A). Through these treatments, thermogravimetric analyses demonstrated that most of the residual impurities in F-CNTFs had been removed (fig. S4), and Raman spectra and x-ray photoelectron spectroscopy (XPS) of F-CNTFs confirmed the functionalization of CNTs (figs. S5 and S6 and table S1) (31). Compared with the pristine fibers, F-CNTFs produced by the purification process exhibited a more compact structure (fig. S7), and the as-obtained fibers subjected to a 12-hour oxidation treatment exhibited an improved tensile strength (fig. S8 and table S1); these fibers were chosen as the raw fibers for further optimization in the following investigation.

When immersed in a CSA bath, F-CNTFs swell by side-wall protonation (fig. S9), which offers plenty of room to rearrange the entangled and porous networks for the improvements of alignment and densification of fibers. By subjecting F-CNTFs to CSA treatment for 10 min with a stretching ratio of 20%, the as-obtained CSA-CNTFs exhibited a substantial

¹Beijing National Laboratory for Molecular Sciences, School of Materials Science and Engineering, College of Chemistry and Molecular Engineering, Peking University, Beijing 100871, China. ²Beijing Graphene Institute (BGI), Beijing 100095, China. ³Institute of Mechanics, Chinese Academy of Sciences, Beijing 100190, China. ⁴School of Engineering Science, University of Chinese Academy of Sciences, Beijing 100049, China. ⁵Department of Engineering Mechanics, School of Civil Engineering, Wuhan University, Wuhan 430072, China. ⁶State Key Laboratory of High-efficiency Coal Utilization and Green Chemical Engineering, College of Chemistry and Chemical Engineering, Ningxia University, Yinchuan 750021, China. ⁷Key Laboratory of Multifunctional Nanomaterials and Smart Systems, Advanced Materials Division, Suzhou Institute of Nano-Tech and Nano-Bionics, Chinese Academy of Sciences, Suzhou 215123, China. ⁸Division of Nanomaterials and Jiangxi Key Lab of Carbonene Materials, Jiangxi Institute of Nanotechnology, Nanchang 330020, China. ⁹School of Nano-Tech and Nano-Bionics, University of Science and Technology of China, Hefei 230026, China.

*Corresponding author. Email: yzhang2011@sino.ac.cn (Y.Z.); wuxianqian@imech.ac.cn (X.W.); enlaigao@whu.edu.cn (E.G.); jianmq-cnc@pku.edu.cn (M.J.); jinzhang@pku.edu.cn (J.Z.)

†These authors contributed equally to this work.

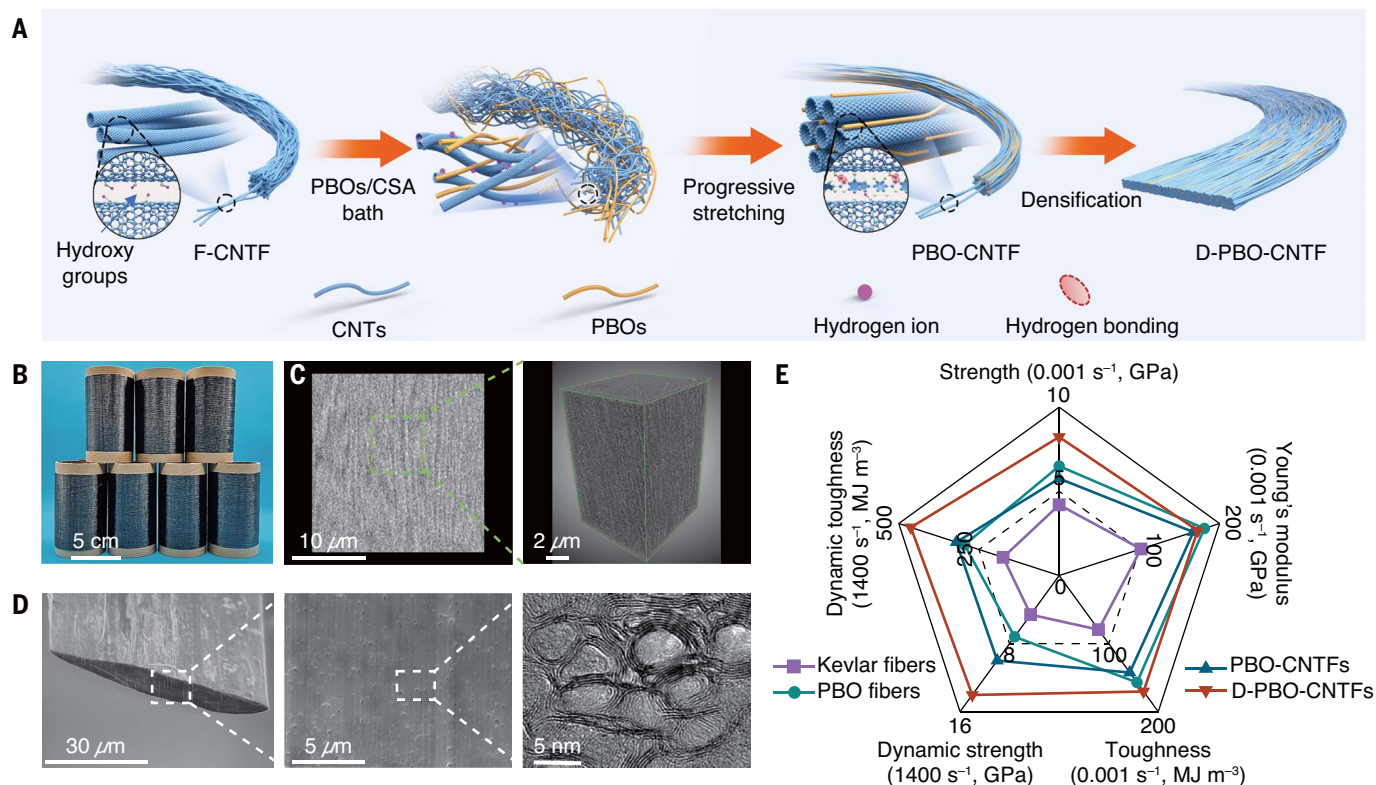


Fig. 1. Preparation, morphology, and mechanical properties of CNTFs.

(A) Strategy to develop highly packed and well-aligned CNTFs. (B) Digital photograph of PBO-CNTF tows. (C) Three-dimensionally reconstructed void microstructure (right) derived from nano-CT results (left) for D-PBO-CNTFs.

(D) SEM (left and middle) and TEM (right) images of the radial cross section of D-PBO-CNTF cut by a focused ion beam. (E) Radar chart for comparing the mechanical performance of different CNTFs and commercial fibers (PBO and Kevlar 29 fibers).

improvement in tensile strength (figs. S10 and S11 and tables S2 and S3). Furthermore, a progressive stretching treatment was introduced. After optimizing the drawing speeds under a certain stretching process, longitudinal scanning electron microscopy (SEM) and transmission electron microscopy (TEM) images showed that the CNTs yield an increase in the alignment along the fiber axial direction (fig. S12). Herman's orientation factor (f) values measured by wide-angle x-ray scattering (WAXS) also support an improvement in the alignment of CNTs. The f for CSA-CNTFs obtained at an optimized stretching rate of 3% per min was 0.90, higher than that of F-CNTFs (0.66) and other fibers prepared at higher drawing speeds (fig. S13 and table S4) (31). This might be because the mechanical treatment at a low drawing speed provides adequate time to disentangle and reorient the CNTs, resulting in the enhancement of tensile strength, Young's modulus, and toughness (fig. S14 and table S5). Solely progressive stretching treatment cannot fully eliminate the voids, as shown in the CSA-CNTFs (fig. S16A). To address this issue, PBOs were infused into CNTFs by uniformly dissolving PBO fibers in a CSA bath at different weight percentages (wt %) (fig. S15) during the progressive stretching treatment. Both the elemental analyses and thermo-

gravimetric analyses demonstrated that PBO-CNTFs treated in the PBOs-CSA solution with a PBO concentration of 0.05 wt % exhibited the highest PBO content (fig. S17 and table S6). Such PBO-CNTFs showed high densification (fig. S16), alignment (Fig. 2A and fig. S18), and mechanical properties (fig. S19 and table S7). Optimal D-PBO-CNTFs were fabricated by applying mechanical rolling on these PBO-CNTFs.

We compared the alignment, densification, and interfacial interactions of F-CNTFs, CSA-CNTFs, PBO-CNTFs, and D-PBO-CNTFs. First, we investigated the alignment of these fibers. The orientation factors measured by WAXS for CSA-CNTFs (0.90), PBO-CNTFs (0.94), and D-PBO-CNTFs (0.92) were higher than that for F-CNTFs (0.66), which is consistent with results of polarized Raman spectra (fig. S20). This indicates that the PBOs-assisted progressive stretching treatment can effectively improve the alignment of CNTs along the fiber axis (Fig. 2, B to D, and table S8). Second, the densification of these fibers was evaluated by small-angle x-ray scattering (SAXS) (32), which indicated that D-PBO-CNTFs have the densest structure (fig. S21). We also reconstructed the microstructures of fibers using nanoscale x-ray computed tomography (nano-CT) and measured

the porosities accordingly (Fig. 2, F and H, fig. S22, and movies S1 to S4). The porosities of F-CNTFs (4.8%), CSA-CNTFs (2.7%), and PBO-CNTFs (1.9%) are higher than that of D-PBO-CNTFs (1.0%). These results are consistent with the cross-sectional SEM images, SAXS characterization, and density measurements (Fig. 2, E and G, and table S9). Third, we explored the interfacial interactions by Fourier transform infrared spectroscopy (FTIR) spectra. The redshift of the hydroxy group peak indicated the hydrogen-bond interactions between CNTs and PBOs (fig. S23A).

Performance of CNTFs

The structural optimization endows the fibers with improvements in quasi-static mechanical properties and electrical conductivities. D-PBO-CNTFs have a tensile strength of 8.2 ± 0.2 GPa, a Young's modulus of 172.7 ± 9.6 GPa, a toughness of 170.3 ± 17.9 MJ m⁻³, and an electrical conductivity of 2.9×10^6 S m⁻¹, which are 4.6, 1.7, 2.1, and 5.8 times those of F-CNTFs (1.8 ± 0.2 GPa, 99.8 ± 7.3 GPa, 82.5 ± 6.4 MJ m⁻³, and 0.5×10^6 S m⁻¹; Fig. 3, A and B, and table S9), respectively. F-CNTFs show an intertube slippage failure morphology, whereas D-PBO-CNTFs exhibit a failure morphology with much fewer pull-out bundles (fig. S24).

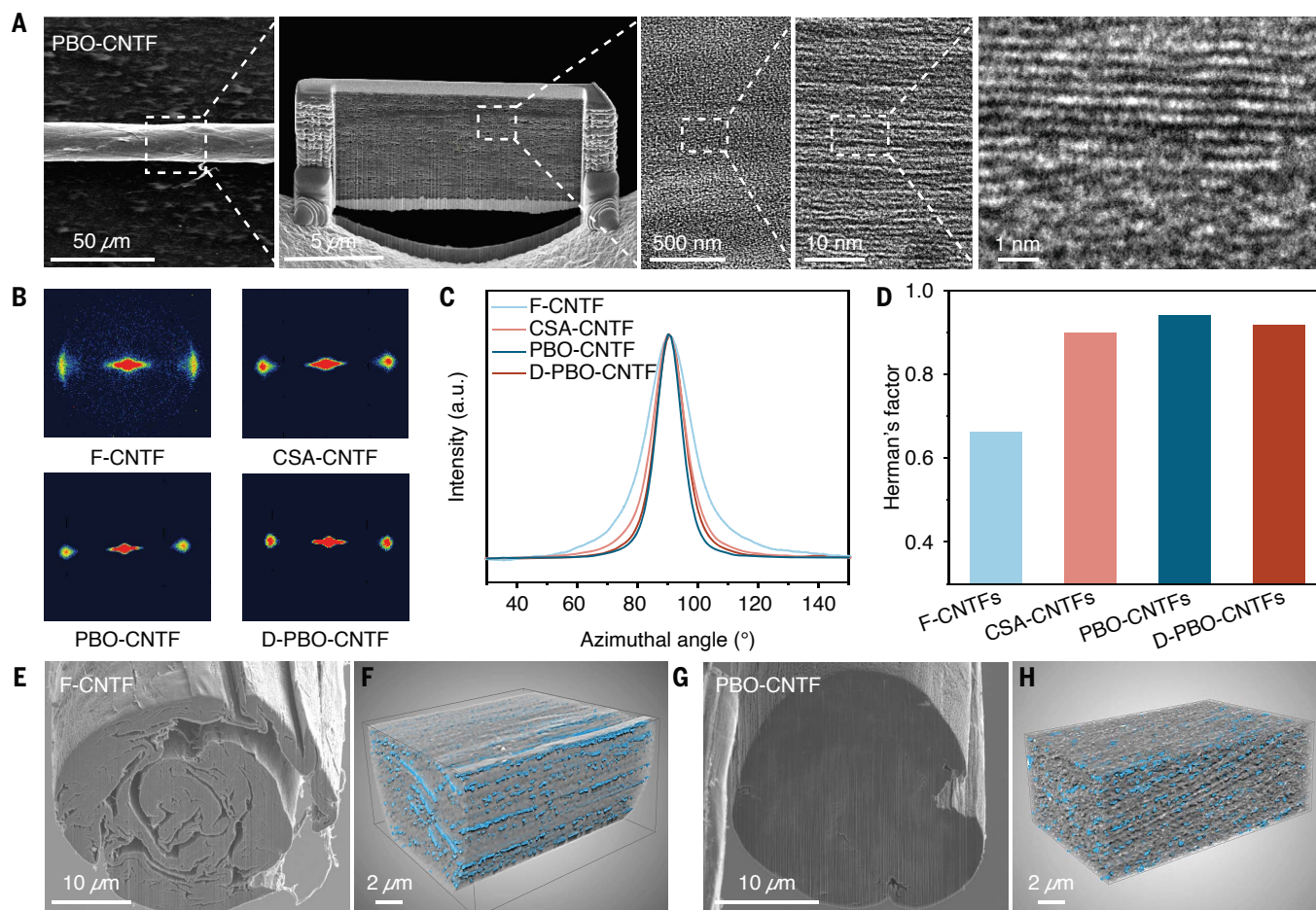


Fig. 2. Structural characterization of CNTs. (A) SEM (two images on the left) and TEM (remaining) images of the axial cross section of PBO-CNTFs cut by a focused ion beam. (B) WAXS patterns of F-CNTFs, CSA-CNTFs, PBO-CNTFs, and D-PBO-CNTFs. (C) Azimuthal intensity profile of different fibers. a.u., arbitrary

units. (D) Comparison of the alignment of CNTs within fibers. (E and G) SEM images of cross sections cut by a focused ion beam for F-CNTFs (E) and PBO-CNTFs (G). (F and H) Three-dimensional void microstructures reconstructed by nano-CT (blue represents the internal voids) for F-CNTFs (F) and PBO-CNTFs (H).

From the ultrahigh quasi-static mechanical properties, we can further estimate the ballistic resistance of fibers via Cunniff velocity (c^*) = $[(\sigma\epsilon/2\rho)(E\rho)^{1/2}]^{1/3}$ (4), where σ , ϵ , E , and ρ are tensile strength, elongation at break, Young's modulus, and density of fibers, respectively. These data show that D-PBO-CNTFs have the best potential for the application of ballistic-resistant materials (Fig. 3C and table S11). It should be noted that c^* is a rough estimation because it depends on the loading rates and local plastic deformation (2). More accurately, the high-strain rate performance of fibers was investigated using a mini-split Hopkinson tension bar (figs. S25 to S27) (3, 31). The shape of stress-strain curves of CNTFs at the high strain rates (Fig. 3D), that is, the stress after the peak value does not drop suddenly, is different from that at quasi-static loading (Fig. 3A). This is because CNTFs have insufficient time to regulate rate-sensitive conformations, such as disentanglement, reorientation, and slippage of nanotubes, thus exhibiting a “cascade-like” breaking of individual CNTs (22, 33). Compared with

the quasi-static strength, D-PBO-CNTFs exhibit a dynamic strength of 9.2 ± 0.8 , 11.0 ± 0.7 , and 14.0 ± 0.7 GPa at strain rates of about 500, 950, and 1400 s^{-1} , which increase by 12.2, 34.1, and 70.7%, respectively. This indicates an improvement in strengthening efficiency as the strain rate increases (table S12). The dynamic strength of D-PBO-CNTFs at a strain rate of about 1400 s^{-1} is 6.1, 2.3, and 1.4 times that of F-CNTFs, CSA-CNTFs, and PBO-CNTFs, respectively (Fig. 3, D and E), and substantially surpasses those of all other high-performance fibers (Fig. 3F and table S12). Meanwhile, the dynamic toughness of D-PBO-CNTFs reaches $462.6 \pm 102.1 \text{ MJ m}^{-3}$ (Fig. 3G), which exceeds that of other high-performance fibers (34, 35). Furthermore, the fracture morphologies show that the intertube slippage of CNTFs at the high strain rates is inhibited, and PBO-CNTFs and D-PBO-CNTFs exhibit a ductile-to-brittle transition in the fracture mode (fig. S28) (22, 31).

To directly assess the impact resistance of these fibers, we performed laser-induced high-velocity transverse impact testing (Fig. 3H and

figs. S31 and S32). The specific energy dissipation power (SEDP) of a single fiber, which is equal to $7.5 \times 10^{10} \text{ kg}^{-1}$ multiplied by its transverse velocity (c_T), is a figure of merit to evaluate its dynamic energy absorption capacity (figs. S29 and S30) (2, 31), where c_T is the transverse velocity. It is challenging to accurately measure the SEDP of D-PBO-CNTFs with a narrow ribbon-like cross section because it depends on the bending resistance along the impact direction (fig. S33 and table S13). Hence, we only compared the SEDP values of the other three fibers. Among these fibers, PBO-CNTFs have the highest SEDP value $[(8.7 \pm 1.0) \times 10^{13} \text{ m kg}^{-1} \text{ s}^{-1}]$ (Fig. 3I and table S14) (2). The impact resistance of PBO-CNTFs is attributed to the high longitudinal wave speed. Finite element simulations demonstrated that the high longitudinal wave speed $[c_L = (E\rho)^{1/2} = 11.4 \text{ km s}^{-1}]$ helps to delocalize the impact energy (fig. S34, A and B), which is consistent with experimental results (fig. S32 and table S14). After the high-velocity transverse impact testing, the craters on the surface of PBO-CNTFs are

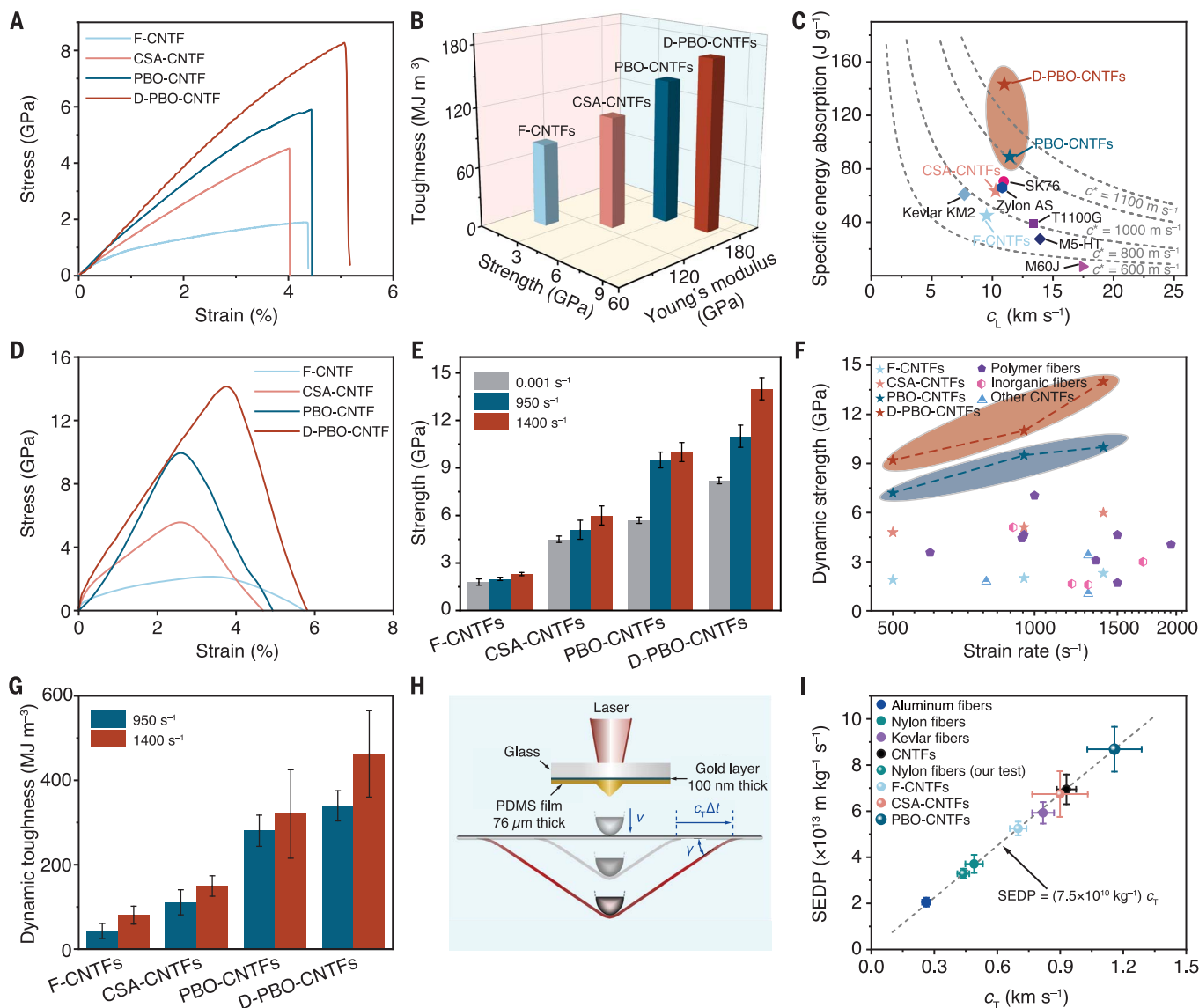


Fig. 3. Mechanical properties of CNTFs. (A) Quasi-static stress-strain curves of F-CNTFs, CSA-CNTFs, PBO-CNTFs, and D-PBO-CNTFs. (B) Comparison of quasi-static tensile strength, Young's modulus, and toughness of different CNTFs. (C) Comparison of specific energy absorption and longitudinal wave velocity of our fibers (indicated by stars) and other high-performance fibers. (D) Stress-strain curves of F-CNTFs, CSA-CNTFs, PBO-CNTFs, and D-PBO-CNTFs at high strain rates of about 1400 s⁻¹. (E) Comparison of the strength of CNTFs at different strain rates. Error bars indicate the standard deviation of the means of independent

measurements. (F) Comparison of the dynamic strength of our fibers and other high-performance fibers at high strain rates. (G) Comparison of the dynamic toughness of CNTFs at different strain rates. Error bars indicate the standard deviation of the means of independent measurements. (H) Schematic diagram of laser-induced high-velocity transverse impact on a single fiber. Here, PDMS, v , Δt , and γ represent polydimethylsiloxane, impact velocity, interval time, and deflection angle, respectively. (I) SEDP values of different fibers. Error bars indicate the standard deviation.

not visible compared with those on CSA-CNTFs (fig. S34, C and D), suggesting that the high dynamic strength of PBO-CNTFs helps to maintain the structural integrity.

Strengthening mechanism of CNTFs

To further determine whether covalent bonds are broken, we measured Raman mapping spectra on the impact region of the fibers and observed an increase in the I_D/I_G value (fig. S37), where I_D is the intensity of D-band and I_G is

the intensity of G-band, which is a signal of bond breaking or atomic rearrangement that also contributes to dissipating energy (2, 36–38). The analyses we describe next show that the simultaneous breakage of CNTs is of central importance to achieving ultrahigh dynamic performance, which results from improvements in interfacial interactions, nanotube alignment, and densification of CNTFs. Regarding the interfacial interactions, we performed experiments using in situ Raman spectroscopy and stress

relaxation. When the applied strain of F-CNTFs is less than 1.3%, the G-band frequency in the Raman spectra shows a small downshift. Afterward, a plateau region extends from 1.3 to 2.5% (Fig. 4A), indicating that the further increase of applied strain does not transfer the stress into CNTs. For CSA-CNTFs, because both the alignment and densification are improved compared with F-CNTFs, the plateau region extends from 2.5 to 3.3% (fig. S38A). By contrast, there is a continuous strengthening stress

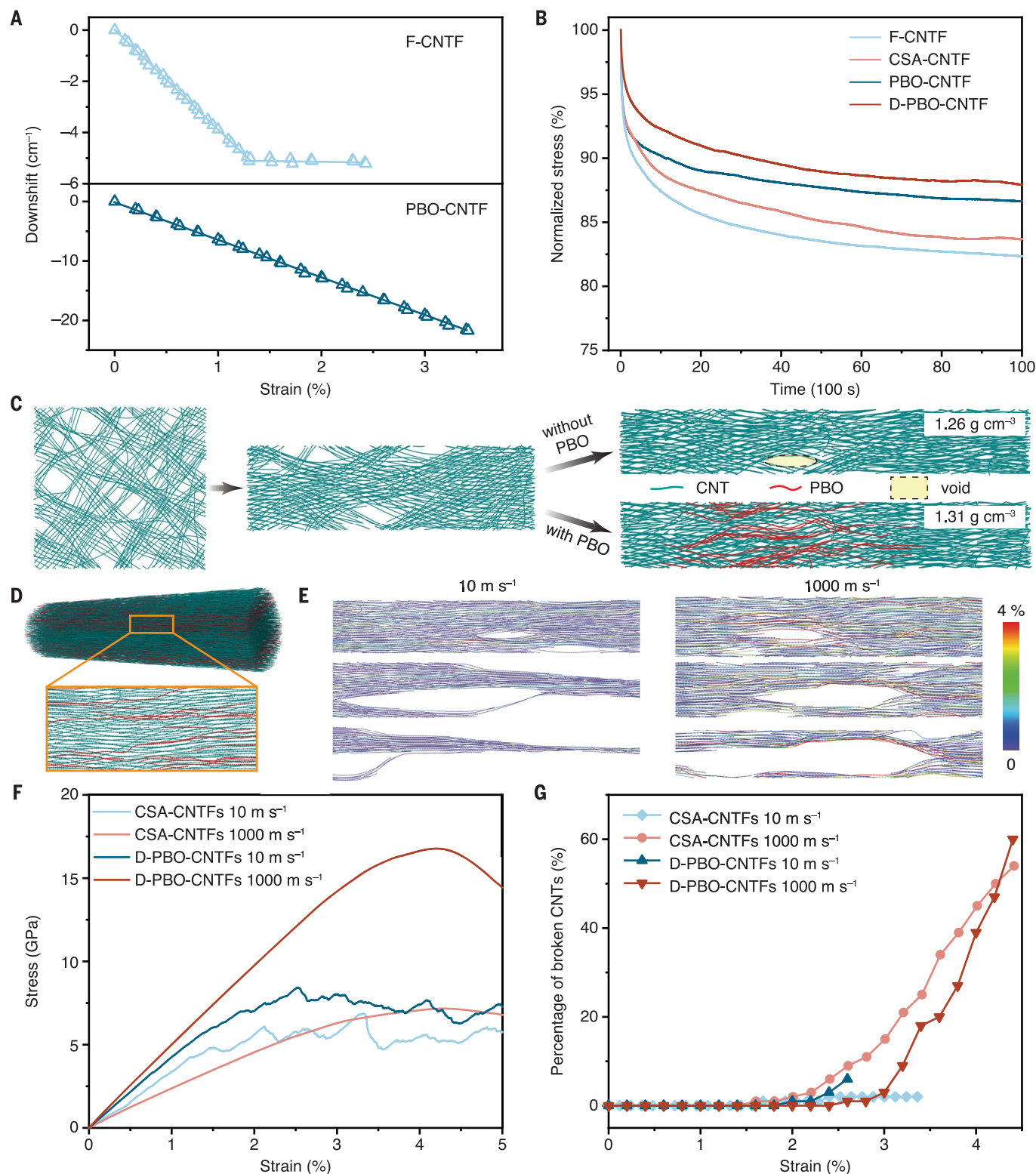


Fig. 4. Mechanistic analyses of the dynamic performance of CNTs.

(A) Dependence of Raman frequency downshifts on the applied strains for F-CNTFs and PBO-CNTFs. (B) Stress-relaxation curves of different fibers at 1.5% strain. (C) Simulation snapshots of progressive stretching treatment for CNTs with and without PBO. (D) Structures and cross-sectional morphology of the simulated model.

(E) Snapshots of deformed D-PBO-CNTFs under low (left) and high (right) loading velocities. The atoms are colored according to the bond strain. (F) Stress-strain curves of CSA-CNTFs and D-PBO-CNTFs under low and high loading velocities. (G) Percentage of broken CNTs for CSA-CNTFs and D-PBO-CNTFs during the tensile process, which is counted up to the peak stress in the stress-strain curves.

transfer to CNTs over the whole strain range for PBO-CNTFs and D-PBO-CNTFs, and the downshift per unit strain is about twice as high in PBO-CNTFs and D-PBO-CNTFs compared with F-CNTFs and CSA-CNTFs (Fig. 4A and fig. S38). Meanwhile, D-PBO-CNTFs show the highest resistance to stress relaxation (Fig. 4B). The increased load transfer efficiency suggests that there are strong interfacial interactions between PBOs and CNTs. We also investigated the interfacial interactions by atomistic simulations. At the nanoscale, our calculations show that the persistence lengths of multi-walled CNTs and PBOs are 1.9×10^6 and 38 nm, respectively, which are generally consistent with prior reports (39, 40). These results indicate that PBOs are much more flexible than CNTs. The discrepancy in flexibility between PBOs and CNTs implies that PBOs would preferentially adsorb onto the rigid CNTs (figs. S39 and S40). The combination of relatively flexible PBOs and relatively rigid CNTs would result in an increased effective contact area. Meanwhile, the interfacial energy between PBOs and CNTs (71.2 meV per atom) is also higher than that between two CNTs (55.5 meV per atom). Consequently, the increased contact area and interfacial energy account for the improvements in interfacial interactions and load transfer efficiency (fig. S41).

We explored the effect of nanotube alignment and densification on the behavior of CNTFs using coarse-grained molecular dynamics (CGMD) simulations. The simulations of progressive stretching treatment show that the fibers undergo a reorganization of microstructures—including curving, reorientation, straightening, and sliding of nanotubes and bundles—toward a more uniform, compact, and ordered structure (Fig. 4C and fig. S42). As shown in Fig. 4C, the voids are observed in CNTFs without the addition of PBOs, whereas these voids are filled in CNTFs with the addition of PBOs. This leads to an increase in simulated densities from 1.26 to 1.31 g cm^{-3} , values that are generally consistent with experimental characterizations of CSA-CNTFs (1.24 g cm^{-3}) and PBO-CNTFs (1.28 g cm^{-3}), as summarized in table S9. Meanwhile, the alignment of CNTs in CGMD simulations is also improved from 0.91 for CSA-CNTFs to 0.93 for PBO-CNTFs, which is attributed to an increased load transfer efficiency due to the addition of PBOs. These simulations are generally consistent with our above experimental characterizations of the alignment and densification. Finally, we did tensile tests of fibers under low and high loading velocities (Fig. 4, D to F). The strain distributions show that the strain primarily localizes at the slippage region under the low loading velocity, whereas CNTs deform more uniformly under the high loading velocity (Fig. 4E). Our simulations demonstrate that the tensile strength of D-PBO-CNTFs under low and high loading velocities is 8.4 and

16.3 GPa, respectively (Fig. 4F). To understand the macroscopic performance of CNTFs under low and high loading velocities, we performed analyses by tracking the microscopic behaviors of each CNT within the fibers. Figure 4G shows that under the low loading velocity, only about 2 and 6% of CNTs within CSA-CNTFs and D-PBO-CNTFs, respectively, break (3I), indicating that the slippage of nanotubes dominates the failure. By comparison, under the high loading velocity, CNTFs have insufficient time to fully regulate rate-sensitive conformations, such as disentanglement, reorientation, and slippage of nanotubes, which results in a high percentage of CNTs breaking. Up to the peak stress, about 54 and 60% of CNTs break for CSA-CNTFs and D-PBO-CNTFs, respectively. The percentage of broken CNTs within CSA-CNTFs is higher than that broken within D-PBO-CNTFs before a strain of about 4%. This is because the inferior structure of CSA-CNTFs leads to stress concentration as well as premature breakage of CNTs. The breakage of CNTs within the D-PBO-CNTFs is much more simultaneous than that within CSA-CNTFs, and the percentage of broken CNTs within the D-PBO-CNTFs becomes larger after a strain of about 4% (Fig. 4G). This simultaneous breakage of CNTs within the D-PBO-CNTFs under a high loading velocity originates from the improvements in interfacial interactions, alignment, and densification, which accounts for the high dynamic strength of these fibers.

Summary

We developed a strategy to fabricate CNTFs with a dynamic strength of 14 GPa. This strategy leads to improvements in interfacial interactions, nanotube alignment, and densification within the fibers. Multiscale analyses combined with experimental evidence revealed that the dynamic performance of CNTFs is primarily due to the simultaneous breakage of individual nanotubes and the exceptional impact-energy delocalization that occurs during the high-strain rate loading process. Our work provides a feasible route to harness the intrinsic strength of individual CNTs at the macroscale to fabricate impact-resistant fibrous materials.

REFERENCES AND NOTES

1. S. Eswarappa Prameela *et al.*, *Nat. Rev. Mater.* **8**, 81–88 (2023).
2. W. Xie *et al.*, *Nano Lett.* **19**, 3519–3526 (2019).
3. J. Luo *et al.*, *Nat. Commun.* **14**, 3019 (2023).
4. Y. Q. Li, H. L. Fan, X. L. Gao, *Compos. Part B* **238**, 109890 (2022).
5. B. Fang, D. Chang, Z. Xu, C. Gao, *Adv. Mater.* **32**, e1902664 (2020).
6. I. A. Kinloch, J. Suhr, J. Lou, R. J. Young, P. M. Ajayan, *Science* **362**, 547–553 (2018).
7. B. Peng *et al.*, *Nat. Nanotechnol.* **3**, 626–631 (2008).
8. Y. Bai *et al.*, *Science* **369**, 1104–1106 (2020).
9. Y. Wen *et al.*, *Nano Lett.* **22**, 6035–6047 (2022).
10. J. Mu *et al.*, *Science* **365**, 150–155 (2019).
11. H. Chu *et al.*, *Science* **371**, 494–498 (2021).
12. C. Chen *et al.*, *Chem. Rev.* **123**, 613–662 (2023).

13. L. W. Taylor *et al.*, *Nano Lett.* **21**, 7093–7099 (2021).
14. N. Behabtu *et al.*, *Science* **339**, 182–186 (2013).
15. S. G. Kim *et al.*, *Carbon* **196**, 59–69 (2022).
16. M. Zhang, K. R. Atkinson, R. H. Baughman, *Science* **306**, 1358–1361 (2004).
17. Y. L. Li, I. A. Kinloch, A. H. Windle, *Science* **304**, 276–278 (2004).
18. H. G. Chae, S. Kumar, *Science* **319**, 908–909 (2008).
19. K. Kozioł *et al.*, *Science* **318**, 1892–1895 (2007).
20. W. Xu, Y. Chen, H. Zhan, J. N. Wang, *Nano Lett.* **16**, 946–952 (2016).
21. J. J. Vilatela, J. A. Elliott, A. H. Windle, *ACS Nano* **5**, 1921–1927 (2011).
22. D. Y. Wang *et al.*, *J. Mech. Phys. Solids* **173**, 105241–105267 (2023).
23. P. F. Wang *et al.*, *Carbon* **102**, 18–31 (2016).
24. X. P. Hu *et al.*, *Compos. Commun.* **28**, 100933 (2021).
25. Y. Jung, Y. S. Cho, J. W. Lee, J. Y. Oh, C. R. Park, *Compos. Sci. Technol.* **166**, 95–108 (2018).
26. J. S. Bulmer, A. Kaniyoor, J. A. Elliott, *Adv. Mater.* **33**, e2008432 (2021).
27. J. Lee *et al.*, *Nat. Commun.* **10**, 2962 (2019).
28. X. Zhang *et al.*, *Sci. Adv.* **8**, eabq3515 (2022).
29. D. Lee *et al.*, *Sci. Adv.* **8**, eabn0939 (2022).
30. Y. J. Wang, S. Xia, H. Li, J. F. Wang, *Adv. Funct. Mater.* **29**, 1903876 (2019).
31. Materials and methods are available as supplementary materials.
32. J. Qiu *et al.*, *ACS Nano* **7**, 8412–8422 (2013).
33. Y. N. Zhang, L. X. Zheng, G. Z. Sun, Z. Y. Zhan, K. Liao, *Carbon* **50**, 2887–2893 (2012).
34. J. Lim, W. W. Chen, J. Q. Zheng, *Polym. Test.* **29**, 701–705 (2010).
35. M. Cheng, W. N. Chen, T. Weerasooriya, *J. Eng. Mater. Technol.* **127**, 197–203 (2005).
36. W. B. Lu, T. Chou, B. Kim, *Phys. Rev. B* **83**, 134113 (2011).
37. N. G. Chopra *et al.*, *Nature* **377**, 135–138 (1995).
38. S. Ozden *et al.*, *Nano Lett.* **14**, 4131–4137 (2014).
39. N. Fakhri, D. A. Tsybolski, L. Cognet, R. B. Weisman, M. Pasquali, *Proc. Natl. Acad. Sci. U.S.A.* **106**, 14219–14223 (2009).
40. D. B. Roitman, M. McAdon, *Macromolecules* **26**, 4381–4383 (1993).

ACKNOWLEDGMENTS

We thank T. Zhou and S. Qu for providing CNTF samples and participating in discussions. We thank H. Lu for helpful discussions. We are grateful for technical support for Nano-X from Suzhou Institute of Nano-Tech and Nano-Bionics (SINAN0), Chinese Academy of Sciences, and Carl Zeiss (Shanghai) Management Co., Ltd. The numerical calculations in this work were done on the supercomputing system in the Supercomputing Center of Wuhan University. **Funding:** This work was supported by Ministry of Science and Technology of China grants 2022YFA1203302 and 2022YFA1203304; National Natural Science Foundation of China grants 52202032, 52021006, T2188101, 52102035, 12272391, and 12232020; Beijing Natural Science Foundation grant 2222094; Strategic Priority Research Program of CAS grant XDB36030100; and Beijing National Laboratory for Molecular Sciences grant BNLMS-CXTD-202001. **Author contributions:** Conceptualization: J.Z., M.J., X.Z.; Methodology: X.Z., X.L., X.J., T.S., J.L., S.X., L.L., D.Y.; Investigation: X.Z., X.L., X.J.; Visualization: X.Z., X.L., and X.J.; Supervision: J.Z., M.J., E.G., X.W., Y.Z.; Writing – original draft: X.Z., X.L., X.J.; Writing – review and editing: J.Z., M.J., E.G., X.W., Y.Z., Y.S., Z.Y. **Competing interests:** The authors declare that they have no competing interests. **Data and materials availability:** All data are available in the main text or the supplementary materials. **License information:** Copyright © 2024 the authors, some rights reserved; exclusive licensee American Association for the Advancement of Science. No claim to original US government works. <https://www.science.org/about/science-licenses-journal-article-reuse>

SUPPLEMENTARY MATERIALS

science.org/doi/10.1126/science.adj1082
Materials and Methods
Supplementary Text
Figs. S1 to S42
Tables S1 to S17
References (41–64)
Movies S1 to S4

Submitted 7 June 2023; resubmitted 29 February 2024
Accepted 10 May 2024
[10.1126/science.adj1082](https://doi.org/10.1126/science.adj1082)